ASM Sc. J., 17, 2022

https://doi.org/10.32802/asmscj.2022.1099

Effect of Methylammonium Iodide on the All-solution Prepared Methylammonium Bismuth Iodide Perovskite Solar Cells Performance

M.F. Achoi[1,2*], S. Aiba[1], S. Kato[1], N. Kishi[1] and T. Soga[1*]

[1]*Department of Electrical and Mechanical Engineering, Nagoya Institute of Technology, Gokiso-cho, Showa-ku, Nagoya, Aichi 466-8555 Japan*

[2]*Faculty of Applied Sciences, Universiti Teknologi MARA (UiTM), Cawangan Sabah, Kampus Kota Kinabalu, Sabah 88997 Malaysia*

The methylammonium bismuth iodide (MBI), a promising lead (Pb)-free perovskite solar cells (PeSC's) material, is suitable for photovoltaic applications due to less toxic and good stability. Herein, the effect of MAI (methylammonium iodide) on the structural, morphological, optical properties and solar cells performance of bismuth-perovskite solar cells (Bi-PeSC's) by all-solution processed multi-step spin coating is investigated. The scanning electron microscope (SEM) morphology visually depicts that with the increase of methylammonium iodide (MAI) precursor molar ratio in bismuth (III) iodide (BiI_3) x [= [MAI]/([MAI]+[BiI_3])] from x=0 to x=0.8, the morphological phase changed significantly. Likewise, the x-ray diffraction (XRD) peak of BiI_3 at 12.78° (003) is tremendously changed in the phase and intensity. At the same time, the solar cell performances exhibit gradual increment as increasing the content of MAI in BiI_3 and the open circuit voltage (V_{oc}) is exceeded four-times of the minimum MAI molar ratio. The maximum V_{oc} obtained by multilayer Bi-PeSC's is 0.34V and an efficiency shows an increment up to 0.0037% at MAI molar ratio, x=0.8. In brief, our findings suggested the improvement of Bi-perovskite absorber layer in the future.

Keywords: MBI; bismuth-perovskites; perovskites solar cells; MAI ratios; Bi-PeSC's

I. INTRODUCTION

To date, the development of solar cells device-based perovskite material has been high demand. Recently, Pb-free perovskites solar cells have attracted much attention, but the efficiency is still low at present. There are several types of Pb-free perovskite solar cells (Pb-free PeSC's) such as $CsSnI_3$, $FASnI_3$, $MASnI_3$, $MA_3Bi_2I_9$, $Cs_3Bi_2I_9$ and many others. Among these, CsSnI3 has recorded the highest theoretical power conversion efficiency (PCE) so far, which is 28.97% as reported in last year (Srivast *et al.*, 2021). However, low stability due to the oxidation of tin is the problem. On the other hand, Bi-based PeSC's are highly stable, but the recorded power conversion efficiency is low at the present. For example, Momblona *et al.* reported 0.04% of PCE in 2020 (Momblona *et al.*, 2020), Shirahata *et al.* in 2020 also had reported the PCE of MBI solar cell of 0.061% (Shirahata *et al.*, 2020) and Park *et al.* in 2015 reported 0.12% of Bi-PeSC's (Park *et al.*, 2015), while the PCE has ever been recorded highest for bismuth-based perovskite solar cells (Bi-PeSC's) is 3.17% in 2018 by Jain *et al.* (Jain *et al.*, 2018). The bismuth-based perovskite ($(CH_3NH_3)_3Bi_2I_9$) (Park *et al.*, 2015) has several advantages such as less toxic (Zhang *et al.*, 2017), good stability (Shin *et al.*, 2018), and low cost (Pujaru *et al.*, 2020). However, many issues have been reported such as incomplete coverage area (Eperon *et al.*, 2014), pinhole (Sarcheshmen *et al.*, 2020), defect (Singh *et al.*, 2016), uniformity and the thickness control (Liu *et al.*, 2018) of the films. These problems are detrimental to the

*Corresponding author's e-mail: faizalachoi86@gmail.com; soga@nitech.ac.jp

performance of lead-free PeSC's device. For example, Singh *et al.* reported that the layer coverage gave a huge impact on the solar cell performances of MBI perovskites (Singh *et al.*, 2016). Besides, Shirahata *et al.* studied the effect of annealing on MBI and found that the surface morphology of Bi-perovskite contains porous structure (Shirahata *et al.*, 2020). Likewise, Sanders *et al.* reported that the MBI suffers from poor substrate coverage surface (Sanders *et al.*, 2018). The main key to the mentioned problems is the solution of the materials precursor. According to Lakhdar *et al.* the solution of materials might detrimental the performance of PeSC's (Lakhdar *et al.*, 2020). Therefore, the effect of MAI precursor molar ratios on the Bi-PeSC's performance is important. Our aim in this work is to improve the surface morphology with uniform Bi-perovskite layer and to clarify the effect of MAI precursor on the photovoltaic properties of solar cells. As per our concern, there is no report on the multilayer Bi-PeSC's at different MAI precursor molar ratios elsewhere.

II. MATERIALS AND METHOD

The substrate and precursor's solution were prepared according to our method previously reported (Achoi *et al.*, 2021). In brief, BiI_3 and MAI dissolved in *N,N*-Dimethylformamide [$HCON(CH_3)_2$] (DMF) solution were stirred at 3000 rpm for preparation of MBI solution with different MAI precursor molar ratios, which varied according to [x= [MAI]/([MAI]+[BiI_3]) 0, 0.1, 0.2, 0.5 and 0.8]. The MBI solution was dripped onto mesoporous titanium dioxide/compact titanium dioxide/fluorine tin oxide (mp-TiO_2/c-TiO_2/FTO) glass surface by using multi-step spin coating method at 1000 rpm for 30 s. The MBI layer is annealed on a hot plate for 10 min at 100 ^oC and then cooled for 10 min. The cooling process was done by displayed the sample inside a petri dish. Furthermore, the whole processes were repeated for eight times to obtain pinhole-free surface of MBI layer. The mp-TiO_2 which acts as electron transport layer (ETL) and poly(3-hexylthiophene-2, 5-diyl) (P3HT) which acts as hole transport layer (HTL), respectively, were prepared via all-solution processed method. First, 0.0469 g of mp-TiO_2 powder diluted in 10 mL of butanol solution to obtain 0.25 M solution, while 0.015 g of P3HT powder was dissolved in 1 mL of dichlorobenzene solution, so that the concentration of P3HT is 15 mg.mL^{-1}. Then, the mp-TiO_2 solution is stirred for 1 h at 800 rpm and left for aging time at room temperature. In the same manner the P3HT solution was stirred. Next, for the fabrication of ETL and HTL, both were fabricated using spin-coating. Furthermore, the mp-TiO_2 is fabricated on the c-TiO_2/FTO at 4000 rpm for 30 s and followed by annealed in furnace chamber for 1 h at 500 ^oC, while for P3HT, the solution is fabricated onto eight layers of a MBI film at 3000 rpm for 20 s and followed by annealed on a hot plate at 120 ^oC for 15 min. Then, both layers were cooled down for 10 min. The cooling process was done by displayed the sample inside a petri dish. The whole process of fabrication was carried out in the N_2 filled glove box. Next, after cooling, the insulator tape (Nichiban polymer tape) with size of 0.3 cm^2 hole in the middle (hole for the silver paste) is displayed with carefully on the top of P3HT layer using a forceps. Then, for the fabrication of carbon electrode, the colloidal graphite was fabricated on the top of insulator tape as displayed earlier using spin-coating at 5000 rpm for 20 s and dried at room temperature for 5 min. Finally, the silver paste is placed onto FTO and deposited carbon layer using a dropper. For the fabrication of carbon electrode, the colloidal graphite, displaying of the insulator tape and silver paste were done outside of the glove box. The purpose of using silver in Figure 7(i) is to provide a better and smooth connection between the I-V probe and the sample (Matiur *et al.,* 2021). The overall full set of fabricated solar cells device structure is shown as in Figure 7(i).

The structural and surface morphology properties of the sample were characterised by X-Ray diffraction (XRD; Rigaku RINT-2100 diffractometer) and the scanning electron microscopy (SEM; JEOL JSM-7600F), respectively. For the XRD, we have used the X-ray radiation source of NI-filtered Cu Kα radiation with wavelength λ = 1.5408 Å and equipped with a Cu target (Rigaku Smartlab). The crystallite of the MBI film was estimated using a Scherrer Equation (1) (Hidzi *et al.*, 2019) as below and in accordance with the input data, as shown in Table 1:

$$D = \frac{k\lambda}{\beta \cos\theta} \quad (1)$$

where, D is average of crystallite size (nm), k is the shape factor (~0.94), λ is X-ray wavelength being used, which Cu

Kα radiation source (λ = 1.5408 Å), β is FWHM (Full width at half maximum) in rad, and β is the peak position or the Bragg's angle (in rad). Noted that for the FWHM value, we obtain from the *Origin2020 software*.

The UV-visible absorption properties were characterised using UV-vis spectrophotometer (JASCO Model V-570). Moreover, we have utilised the Raman spectroscopy (JASCO NRS-1500W) at room temperature with an excitation wavelength of 532 nm to confirm the existence of any impurities of the fabricated films and as validation to the XRD measurement. Finally, the thicknesses of MBI layer were measured using the Dektak machine (Veeco-Dektak150).

The performance of the device has been recorded using a solar simulator with white light illumination at AM: 1.5 and 100 mW.cm^{-2} conditions and measured by using a 238 Keithley high current source. The measurement conditions were done in a scan rate of 50 mV/s and 0.01 V voltage step, with an illumination area through a carbon surface area of 0.16 cm^2 as a single measurement without light soaking, in combination with a Xenon Lamp (Jasco, XCS-150) power supply sun simulator (Jasco, Model PS-X500), which was calibrated to AM1.5 standard conditions by using an Oriel 91,150 V reference cell.

III. RESULT AND DISCUSSION

A. Structural Analysis

Figure 1 shows the XRD curves of MBI layers at different ratios of MAI precursor ratio. All the MBI peaks are indexed as hexagonal structure with space group P63/mmc except x=0 (a), using the Joint Committee on Powder Diffraction Standards (JCPDS) card No. 01-070-0666 (Ataei *et. al.*, 2021; Shirahata *et al.*, 2020). At lower MAI ratio (x=0) in Figure 1(a), the peak of BiI_3 at 12.78° (Wang *et al.*, 2017) appeared as a dominant, sharp and strong intensity peak, which is assigned to (003) lattice planes, while another three peaks are assigned to a very low intense of FTO peak, which are at 26.82° (Shirahata *et al.*, 2020), 33.91° (Shirahata *et. al.*, 2020; Sanders *et al.*, 2019), and 38.06° (Wang *et al.*, 2020). Another two peaks can be observed at 29.60° (012) and 31.7° (110), which were assigned to Bi_2O_3 and BiOI, respectively. These two less intense peaks were formed in a MBI multilayer due to the reaction to the residual oxygen in nitrogen gas or air exposure during XRD measurement even the deposition process was carried out in nitrogen filled glove box, as reported by Hoye *et al.* (Hoye *et al.*, 2016). Furthermore, one peak of TiO_2 with a broad peak is observed at 25.37° (Wang *et al.*, 2017) and at the same time, no MBI peak is observed. As for increased the ratio of MAI from x=0 to x=0.1, the peak of BiI_3 is changed to MBI peak at 12.67° (Li *et al.*, 2017) and decrease in intensity as shown in Figure 1(b). As can be seen that the peak of BiI_3 a bit shifted to the left-side from 12.78° (BiI_3) (Lakhdar *et al.*, 2020) to 12.67° (MBI) (Li *et al.*, 2017), which corresponds to the (003) and (101) lattice planes of BiI_3 and MBI, respectively, while another three peaks of FTO and one peak of TiO_2 remains as previously. It means that the MBI phase replaced BiI_3 as the main phase in Bi-PeSC's. To support this explanation, it can be seen in the inset Figure 5i (a and b), the colour of as-prepared sample is changed from deeper black colour (BiI_3) to black colour as the introduction of MAI precursor into BiI_3. B.-M. Bresolin *et al.* and Z. Zhang *et al.* reported that almost BiI_3 has been transformed completely into MBI which is implying the certain reaction occurred after the addition of the MAI into BiI_3 resulted in changing of colour (Zhang *et. al.*, 2017; Bresolin *et al.*, 2019). As for increased the ratio of MAI to x=0.2, the peak of MBI at 12.67° (101) and the TiO_2 peak at 25.37° start to decrease in intensity (Wang *et al.*, 2017) as shown in Figure 1(c). On the other hand, one peaks of a MAI can be seen at 35.23°. At the stage of x ≥ 0.5, MBI peak at 24.58° (006) starts to dominated in the multilayer MBI as shown in Figure 1(d) and 1(e). However, the peak at 12.67° (101) (Li *et al.*, 2017) becomes a very weak intensity and a broad peak. At the same time, two of MAI peaks are observed at 29.12° and 35.23°. Finally, at x=0.8, two peaks of MBI, which at 12.67° and 24.58 (Hoye *et. al.*, 2016; Shirahata *et al.*, 2020) were observed, whereby a MBI peak at 12.67° almost disappeared while now the MBI peak at 24.58° (006) appeared as a high and dominant peak than TiO_2 peak as shown in Figure 1(e). Then, another three new peaks were appeared with low intensity and broad peaks, at 19.73°, 39.79° and 40.60°, which were assigned as MAI peak and same as reported in ref. (Levchuk *et al.*, 2016). To confirm that, in the inset of Figure 5(i) (d-e) shows that the colour of sample was

changed from orange colour to lighter orange colour (Ran *et al.*, 2017). This changing of colour proves that the existence of MAI in BiI_3 phase and it influences the optical properties and the performance of Bi-PeSC's. This will be further described in the UV-vis absorption properties and solar cells performance section.

Table 1. The Scherrer equation input data of the MBI peak

MAI ratios	θ Braggs Angle*	θ (In Rad)	β (FWHM)	B (FWHM) Rad unit	cos θ	*D* (nm)
(a) x=0	6.38	0.11135	0.37381	6.5242 x 10^{-3}	0.9999	22.2
(b) x=0.1	6.34	0.1106	0.39099	6.8241 x 10^{-3}	0.9999	21.2
(c) x=0.2	6.34	0.1106	0.40545	7.0764 x 10^{-3}	0.9999	20.5
(d) x=0.5	12.28	0.2142	0.43910	7.4892 x 10^{-3}	0.9999	19.3
(e) x=0.8	12.28	0.2142	0.45321	7.9100 x 10^{-3}	0.9999	18.3

**Dominant peak*

Furthermore, from Figure 1, the crystallite size (*D*) of MBI PeSC's was calculated using *Scherrer's* equation (Dhaouadi *et al.*, 2018) as shown in Figure 2(i) and Table 1. The purpose of measuring the *D* value is to clarify the relationship of photovoltaic properties with *D* value, beside to clarify it influence on the changing of morphology and the effect of MAI on *D* value. Figure 2(i) exhibits that the *D* decreases with increasing the MAI precursor molar ratios, while Figure 2(ii) is the thickness for different MAI ratio, whereby the thickness of MBI layer decreases as well. The thickness decrease is due to the lower BiI_3 concentration of the precursor solution at higher x value. Both are affected by changing amount of MAI from x=0 to x=0.8. As an introduction of MAI in BiI_3 causes the *D* decreases from 22.2 nm to 18.3 nm. According to Bresolin *et al.* the *D* is decreasing from 200 nm to 50 nm due to the introduction of MAI (Bresolin *et al.*, 2019). This report is in line with our result of *D* value, which shows the decrement. Furthermore, it is expected that the MAI being introduced into BiI_3 will improved the morphology of MBI perovskite film that will be discussed further in the next SEM section. Besides, Jain *et al.* reported that the formation of MBI film after the reaction between BiI_3 and MAI, changes in the grains size (Jain *et al.*, 2018). Our results agree with this finding and it is proved that the quality of our MBI layer is improved as shown in Figure 4, which will be discussed in the next SEM morphological section. Meanwhile, the relationship between *D* values and thickness with the short circuit current density (J_{sc}) will be further explained in the next solar cells performance section. In brief, an introduction of MAI in BiI_3 significantly affected the crystallinity, crystallite size and the crystal phase of MBI.

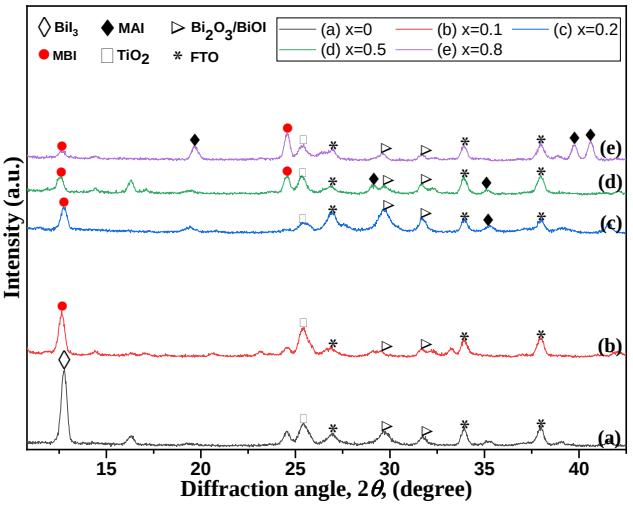

Figure 1. XRD curves of Bi-PeSC's at different MAI ratios

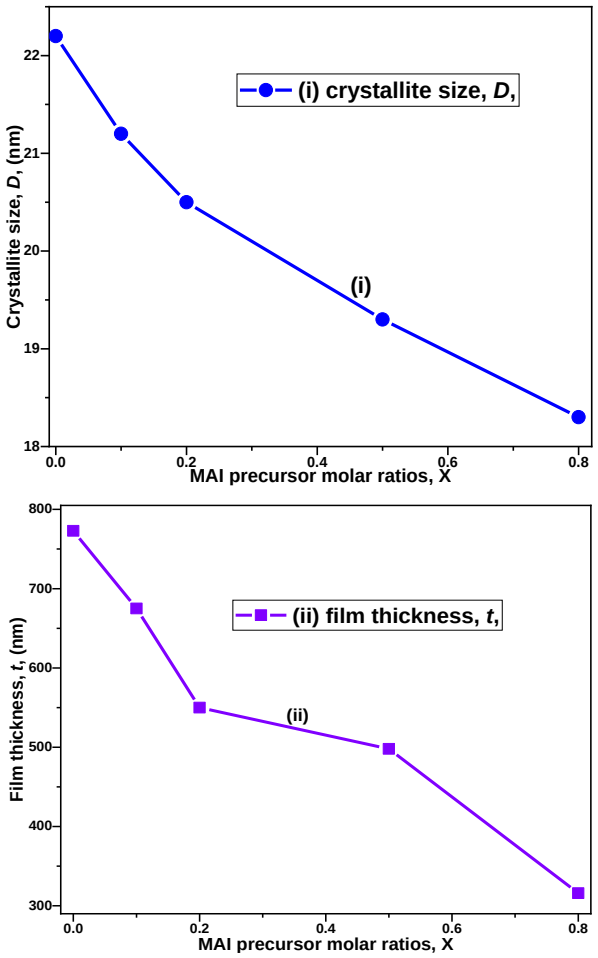

Figure 2. The variation of (i) *D*, and (ii) thickness against MAI ratios

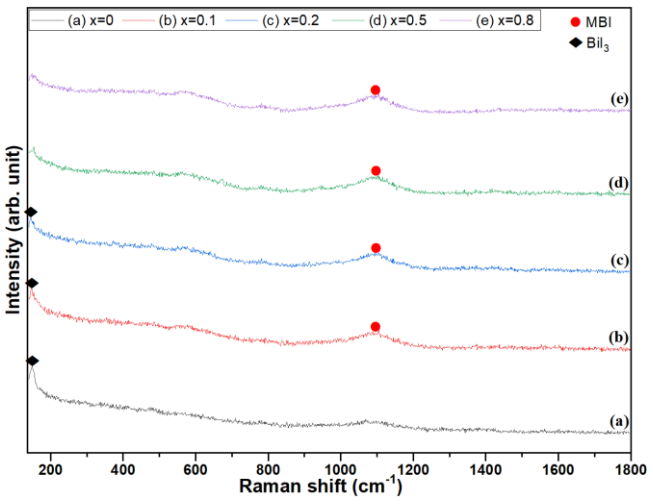

Figure 3. Raman Spectra of Bi-perovskite at different amount of MAI

Furthermore, the Raman spectroscopy was performed to confirm the structures and impurities of the fabricated film and as validation to the XRD measurement. Figure 3 shows the Raman peak of BiI_3 and MBI at different of MAI precursor molar ratios, x. Basically, Raman peak of BiI_3 and MBI were recorded at Raman shift of 159 cm^{-1} and 1096 cm^{-1}, respectively (Chen *et. al.*, 2018; Jain *et al.*, 2018). Our result is similar to the reported (Jain *et al.*, 2018), which indicates that BiI_3 and MBI peaks only are detected by Raman spectroscopy, and no MAI peak is detected which indicated the complete conversion of BiI_3, as can be seen in the Figure 3(e) and Equation (2). At x=0 of MAI, we can see the Raman shift of BiI_3 is high in intensity with a narrow peak, and then gradually becomes low in intensity at x=0.1 and x=0.2, as can be seen in Figure 3(b) and (c), respectively. Finally, the Raman shift of BiI_3 is disappeared at x=0.8, as shown in Figure 3(e). It means the BiI_3 completely reacted with the MAI to a MBI as in Equation (2), which recorded at Raman shift of 1096 cm^{-1}, and this is in good agreement with XRD result in Figure 1, which indicates no BiI_3 peak is shown in Figure 1(e). In general, we can observe that the Raman peak of BiI_3 at 159 cm^{-1} is changing in intensity, as an introduction of MAI into BiI_3 from x=0 to x=0.8, while the MBI Raman shift at 1096 cm^{-1} remained unchanged. The Raman characterisation was performed three times to confirm the validity of output result. Additionally, according to Jain *et al.* no FTO peak is detected in their Raman result (Jain *et al.*, 2018), which indicates MBI layer well covered the FTO surface and it supported by eight layers of MBI. In addition, no impurities such BiOI and Bi_2O_3 are detected. This shows that the Raman characterisation is accurate and powerful to detect impurities and other peak. In brief, via Raman spectroscopy, we confirm that there are no impurities in our sample or might be less of contamination, and it is proof that the introduction of MAI significantly affected the structural properties of MBI films.

B. Morphological Properties

Figure 4 visually depicts the SEM images of Bi-PeSC's at different MAI ratios. At x=0, it can be seen that a bunch cluster of BiI_3 appeared as a white colour agglomerated and accumulated to each other as confirmed by XRD result. The BiI_3 is dominated and appeared as a main phase in Bi-PeSC's as shown in Figure 4(a). The formation of a bunch cluster of BiI_3 is due to the nucleation process and grain growth reported by Kubota *et al.* and Im *et al.* (Kubota *et.*

al., 2001; Im *et al.*, 2014). As increasing the MAI ratios from x=0 to x=0.1, the morphological phase absolutely changed from a bunch cluster of BiI_3 to a small size of single particle that separately to each other as shown in inset Figure 4(b). This changing in morphological phase was correlated to the grain growth process that happened at low concentration as reported by Im *et al.* (Im *et al.*, 2014) and after the reaction between two precursors, BiI_3 and MAI as shown in Equation (2). In accordance to XRD result, MBI takes over the BiI_3 phase as a main phase in Bi-Perovskite. It thus elucidates that the reaction between two precursors occurred and then led to the formation of a MBI. At x=0.2 in Figure 4(c), the MBI particles start to form a clear image of agglomerated MBI particle with a big size and close to each other. According to Lan *et al.* the formation of an enlarged MBI grain in the films due to the lattice mismatching between BiI_3 and MBI created a non-homogeneous surface morphology of the films (Lan *et al.*, 2017).

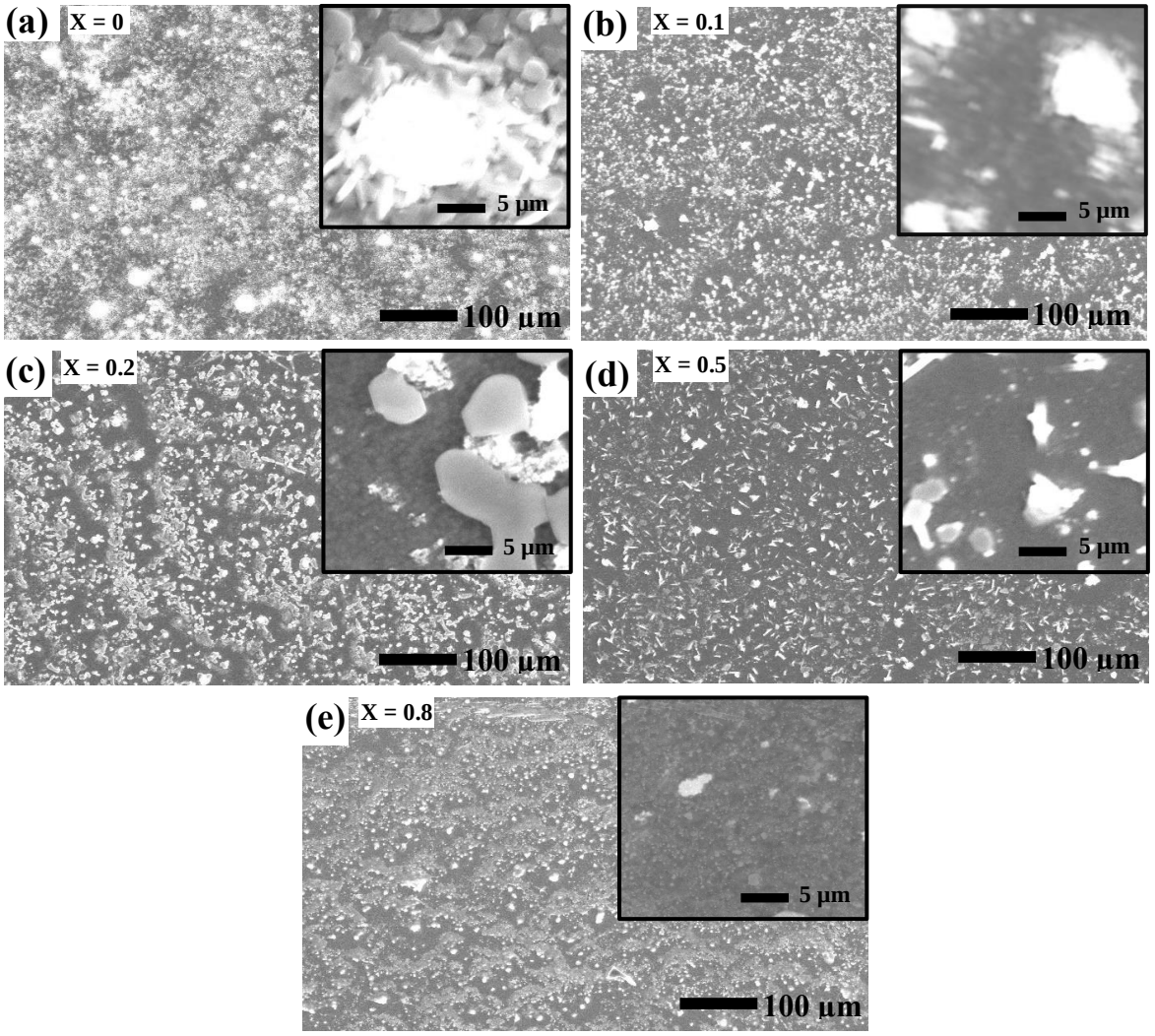

Figure 4. The morphologies properties of Bi-PeSC's at different MAI ratios. Insets are magnified surfaces.

This explanation confirmed that our sample is non-homogeneous surface as shown in inset Figure 4(c). As for further increases the MAI ratios to x=0.5, it can be seen clearly that a white particle discretely distributed and discontinuous to each other. In addition, no an agglomeration of particle with big-size are seen. Finally, an increment of MAI ratios to x=0.8, the SEM images visually depicts that the agglomerated and accumulated particle completely disappeared, which resulted in the morphological absolutely change. According to Lan *et al.* the MBI dominated in the Bi-perovskite films, which correspondingly the surface morphologies were totally changed (Lan *et al.*, 2017). Our result agree with this report, as a MBI dominated in Bi-PeSC's as confirmed by XRD

result in Figure 1(e). In addition, the surface become continuous, uniform, and better coverage surface. On the other hand, a very low intensity of XRD peak for Bi_2O_3 and BiOI were observed, which also might attribute to the continuous and uniform surface of a MBI layer as shown in Figure 1(e), because Hoye *et al.* reported that the formation of Bi_2O_3 and BiOI is due to air exposure, which might lead to the discontinuous and inhomogeneous surface of a film since both oxidised bismuths created a large crystal in a film (Hoye *et al.*, 2016). In addition, according to Stumler *et al.* the formation of Bi_2O_3 and BiOI cannot be avoided and it might happen during the deposition process (Stummler *et al.*, 2019). Besides, the other possibility that contributes to this formation is during the displaying of insulator tape and the fabrication of carbon layer outside the glove box.

$$2BiI_3 + 3\mathrm{CH_3NH_3I\,(MAI)} \rightarrow (CH_3NH_3)_3Bi_2I_9(MBI) \quad (2)$$

In summary, an increment of MAI ratios in BiI_3 significantly influenced the morphologies of Bi-PeSC's.

C. Optical Properties

Figure 5(i) shows the UV-vis absorption spectra and photographed images of MBI layers with changing of MAI ratio from x=0 to x=0.8, while Figure 5(ii) shows the UV-vis absorption spectrum of pure MAI film (x=1.0). At x=0, the fabricated layer shows a deeper black colour. It means that it has absorption peak same as those of BiI_3 films as reported previously by Jain *et al.* (Jain *et al.*, 2018) and Sanders *et al.* (Sanders *et al.*, 2018). The BiI_3 layer (optical bandgap of around 1.75-1.90eV) has a broad absorption from 450 nm to 710 nm, and the absorption edge interpolated to 710 nm (1.75 eV), agrees well with the reported result (Jain *et. al.*, 2018; Sanders *et. al.*, 2018; Ran *et al.*, 2017). The shoulder at 710 nm decreases with increasing the MAI ratios. It means that the electronic transition happened between two bands according to Jain *et al.* (Jain *et al.*, 2018). After the addition of MAI into Bi-perovskite at x = 0.1, the colour of the layer starts to change from a deeper black colour to a black colour. This indicates that the reaction starts to happen between BiI_3 and MAI to form a MBI as shown in Figure 1(b) and Equation (2). On the other hand, the absorbance intensity is decreased as shown in Figure 5(i)(b). At x=0.2, the colour of a layer changed from black colour to deeper orange colour as shown in Figure 5(i)(c). Meanwhile, the samples at x=0.1 and x=0.2 show a strong absorption peak at around 500 nm, which has optical bandgap energy about 2.1 eV, as shown in Figure 6(b) and (c), and our result is in agreement with the previous reported work (Ran *et al.*, 2017), which explained that the electron transition of $^1S_0$ to $^3P_1$ to $^3P_2$ (Sanders *et al.*, 2018), which stated of the trivalent Bi^{3+} in the $[Bi_2I_9]^{3-}$ bioctahedrons (Kawai *et al.*, 1996) when light energy increased (Oz *et al.*, 2016). Besides, the higher absorption peak indicates that the charge transport is enhanced and thus reduced the recombination losses (Shin *et al.*, 2018). As for further increase the MAI ratios to x=0.5, the colour of sample further changed from deeper orange colour to orange colour. It means that the thickness of film also changed, and at the same time the absorption is decreases, as shown in Figure 2(ii) and Figure 5(i)(d). According to Ran *et al.* the colour of the film was lighter, so the thickness of the MBI film was low as well (Ran *et al.*, 2017). Finally, at x=0.8, the colour of the MBI layer turned into lighter orange, as shown in Figure 5(i)(e) and then resulted in further decreasing of thickness of MBI layer as shown in Figure 2(ii). However, the absorption of a layer decreases and the absorption wavelength region was shifted to the left-side, which from 500 nm to 477 nm due to amount of MAI-added into MBI perovskite is high. According to Sanders *et al.* and Limaye *et al.* the low absorption is attributed to the crystallographic defects that is created states in the bandgap, which finally resulted in a low absorption of photons with sub-bandgap energy (Limaye *et al.*, 2015). Besides, the lower absorption means a quick transformation of BiI_3 to $(CH_3NH_3)_3Bi_2I_9$ as reported by Jain *et al.* (Jain *et al.*, 2018). In case of our study, if comparing with the UV-vis absorption of x=1.0 of MAI as shown in Figure 5(ii), it clearly shows that the peak at around 477 nm and other two peaks (red arrow mark) contribute to the MAI absorption peak. It thus elucidates that the MAI influence the light absorption shift of Bi-PeSC's. In brief, from the colour of samples, it shows that at low MAI ratio (x=0), a darker film is obtained (Sanders *et al.*, 2018), and at the highest MAI ratio (x=0.8), a lighter film is obtained instead. It means that the changing of colour sample is relying on the layer thickness also, as the

incorporation of MAI in BiI_3, as shown in the Figure 5(i) and Figure 2(ii).

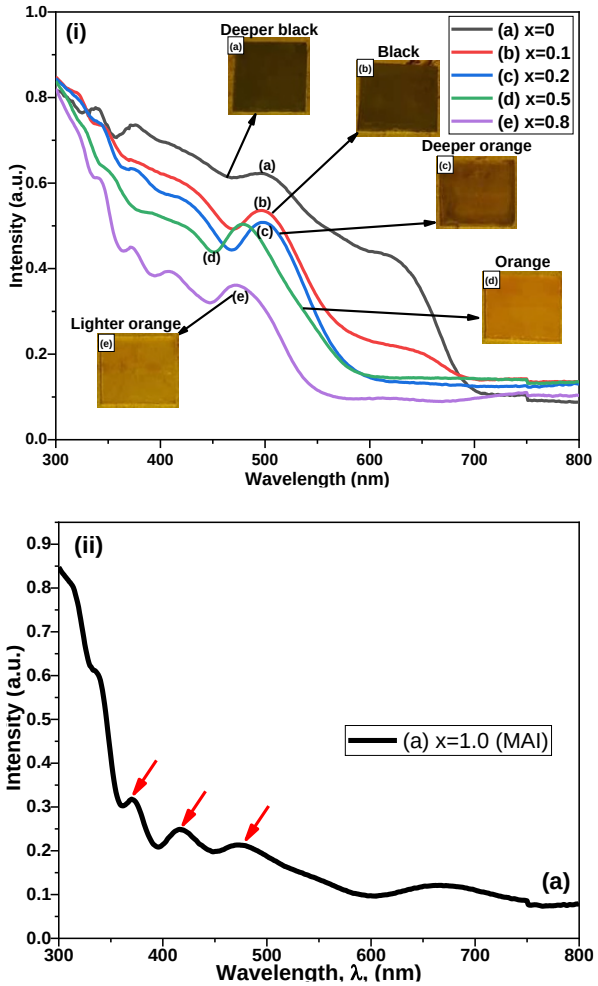

Figure 5. (i) UV-vis absorption spectra of Bi-PeSC's at different MAI ratios. Inset photographed images, (ii) absorption spectrum of MAI

It influenced the solar cells performance as previous reported work (Ran *et al.*, 2017). This will be further discussed in the next photovoltaic section.

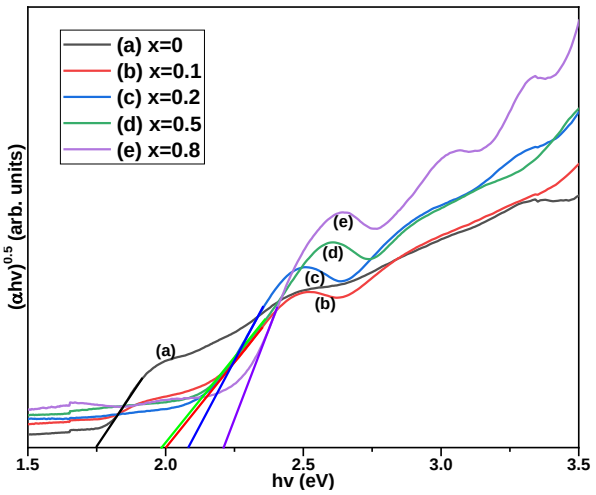

Figure 6. The *Tauc's plot* of Bi-PeSC's at different MAI ratios

Figure 6 indicates the Tauc's plot of MBI at different ratios of MAI. The optical band gap (E_g) was calculated from the absorption spectra shown in Figure 5(i) using a Tauc plot. It can be observed the E_g is shown around 1.98 eV~2.21 eV, for sample with MBI, while without MAI, optical bandgap is 1.75 eV, for BiI_3. It is well known that BiI_3 has a narrower bandgap as reported by Ran *et al.* (Ran *et al.*, 2017). At high amount of MAI, at x=0.8, the E_g is 2.21 eV as shown in Figure 6(e), which is similar to the reported (Ran *et al.*, 2017). However, at a moderate amount of MAI, x=0.5, E_g is 1.98 eV, as can be seen in Figure 6(d). The changing of E_g as result from added-MAI is encouraged by the large dieletric mismatch between the large organic MA^+ cation and isolated $Bi_2I_9^-$ after the reaction both ion to form a $MA_3Bi_2I_9$ and then resulted in the interlayer crystal of MBI (Jain *et al.*, 2018). Thus, it is expected to contribute a significant role in charge transport. In brief, the E_g of MBI film is significantly affected after the introduction of MAI into BiI_3.

D. Solar Cells Performance

Figure 7 shows the solar cells performance of Bi-PeSC's while inset Figure 7(i) shows the architecture design of Bi-PeSC's, and Table 2 is the summary of solar cells parameters. At x=0 in Figure 7(a), the open circuit voltage is 0.08 *V*. As for changed the ratio to x=0.1, the V_{oc} is increased almost double value (0.14 V) with 0.0019% efficiency of solar cells as shown in Figure 7(b). As for increased the MAI ratio to x=0.2, V_{ic} is continuously increased almost double value

again to 0.22 V and the efficiency (0.0029%) is increased as shown in Figure 7(c). The J_{sc} and V_{oc} values for the sample x=0 are extremely small because it is not MBI film but BiI_3 film as shown in Figure 1. The short-circuit current, J_{sc}, starts to decrease before showing the fluctuating trend between x=0.2 and x=0.8. But the V_{oc} value is showing the trend of continuous increment as seen earlier, and as shown at x=0.5. Further increases the MAI ratio to x=0.8, Figure 7(e) shows that the J_{sc} decreased from 44 to 36 μA/cm². Yet, the V_{oc} is still further increased exceed four times of the minimum MAI ratio (x=0). An increment of V_{oc} value is due to the better morphology with improved interface layer as reported by Ataei *et al.* (Ataei *et al.*, 2021) as shown in Figure 4, while for the decreasing of J_{sc} might be occurred due to the four possible reasons that might be considered. According to Zhang *et al.* the film defect such as impurities or grain boundaries, might contribute to decreasing of J_{sc}, due to the charge recombination in solar cells film (Zhang *et al.*, 2015). The second reason is the crystallite size, *D*. The decrease of *D* as increasing MAI ratios led to the increase of high surface area, which encouraged to possibility created some structural defect, in other word, the *D* may affect the morphological film, which results in incompletely coverage and less homogeneity of a film and as a result, it may also affect to the performance of solar cells. According to F. Unlu *et al.* less homogeneity of the film may result in poor of interface connection between perovskite layer and ETL and consequently facilitating poor charge transport, thus leading to the low J_{sc} value (F. Unlu *et al.,* 2020). While Sanders *et al.* studied the concentrations of the perovskite precursors solution and reported that the crystallites size has a major influence on the PV performance and mentioned that higher PCE can be achieved by improving its coverage (Sanders *et al.*, 2018). As discussed earlier in the XRD result, an increment amount of the MAI ratios in BiI_3 the crystallite size slowly decreased and consequently, the J_{sc} is decreased because the structural defect density is increased, as shown in Figure 7. It means that the difficulties of electron diffusion via an active layer creates a charge carrier (electron) mobility became worse. The third reason is the penetration of MBI into a TiO_2 layer. Stummler *et al.* reported that in the fabrication of MBI layers by employing MAI, the penetration of MBI into the TiO_2 could be the reason for higher short-circuit currents (Stummler *et al.*, 2019). Instead, poor penetration into a TiO_2 layer resulted in low short-circuit currents of a solar cells. Moreover, a high MAI ratio causes the decreases of crystallites sizes. Shirahata *et al.* have found that the small-sized crystallite MBI contributed to the high voltage but a bit low current, and they mentioned it is due to the small-sized MBI crystallites which suppressed electron-hole recombination in the cells (Shirahata *et al.*, 2020). Our finding agrees well with this report, that the small-sized crystallite sized resulted in being a high V_{oc} and efficiency, which 0.34 V and 0.0037 %, respectively. But it produces a bit low of short-circuit current compared to others sample, as shown in Table 2. The fourth reason is the decreasing of the MBI thickness which produces small photo absorption, resulting in the decreasing of J_{sc} value as well. Furthermore, in Figure 8, the J_{sc} value decreases with MAI ratio from x=0.2 to x=0.8, while the thickness also decreases, as shown in Figure 2(ii). At high MAI ratio (x=0.8) the thickness of MBI layer decreased to 316 nm, as a result, J_{sc} value is decreased. The above reasons produce high resistance MBI layers, which results in the small J_{sc}. The I-V curves shown in Figure 7 support that the series resistance of PeSC's is high from the slope of I-V curves at current is zero. It is known that high series resistance degrades the short circuit current of solar cell seriously (Green, 1982). After this clarification, we can conclude that the factor that might contribute to our enlargement of solar cell efficiency of Bi-PeSC's device is due to a better film morphology resulted in a better voltage (Ataei *et al.*, 2021) with a good fill factor (FF), as shown in Figure 4 and Table 2, besides in accordance with this Equation (3).

$$PCE = \frac{V_{oc} \times J_{sc} \times FF}{P_{in}} \quad (3)$$

where, P_{in} is incident light power density. This equation elucidates that beside the J_{sc} value, a better of V_{oc} and FF also contibute to the enlargement of efficiency value.

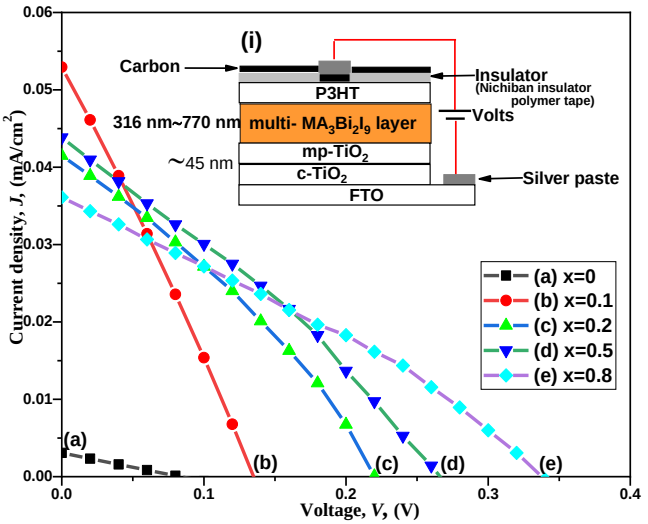

Figure 7. I-V curves of Bi-PeSC's for different MAI ratios

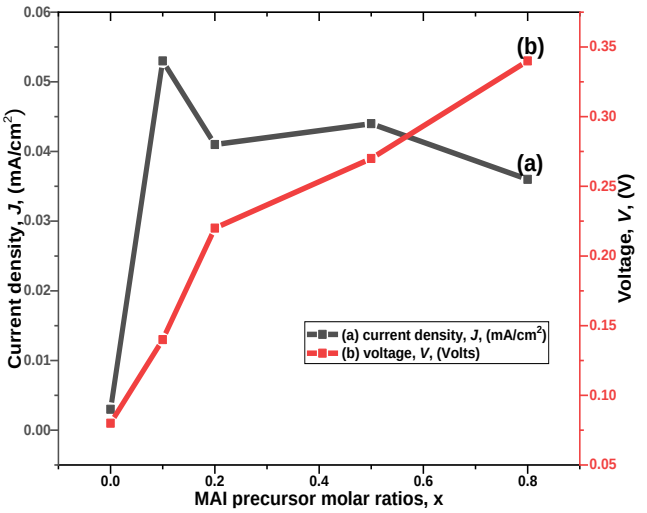

Figure 8. The relationship of short-circuit current, J_{sc}, and open circuit voltage, V_{oc}, for different MAI ratios

It thus elucidates that the introduction of MAI significantly influences the performance of Bi-PeSC's, which resulted in a high V_{oc}, but reduced J_{sc} as can be seen in Figure 8.

Table 2. The performance of Bi-PeSC's at different of MAI ratios

MAI ratios	J_{sc} (mA/cm²)	V_{oc} (volts)	FF (%)	PCE (%)
(a) x=0	0.003	0.08	24.5	0
(b) x=0.1	0.053	0.14	26.4	0.0019
(c) x=0.2	0.041	0.22	31.5	0.0029
(d) x=0.5	0.044	0.27	29.7	0.0035
(e) x=0.8	0.036	0.34	30	0.0037

IV. CONCLUSION

We successfully fabricated the multilayer Bi-PeSC's devices with changing the MAI precursor molar ratios ([MAI]/([BiI_3] + [MAI])) via all-solution processed multi-step spin coating. The voltage and power conversion efficiency were increased with increasing the MAI precursor ratios to 0.8. However, the J_{sc} value is a bit low due to the high resistance and the thickness of MBI layer, while the SEM images visually depicts a continuous, uniform, homogeny, non-agglomerated and good coverage of a MBI layer at =0.8 of MAI ratios and this resulting a high value of V_{oc} in our sample. The XRD result shows that the crystallite size is 18.3 nm at x=0.8. Hence, at high ratio of MAI in BiI_3 significantly influenced the structural, morphology, optical properties and the performance of Bi-PeSC's.

In summary, a too-lower of MAI composition is not reasonable. Thus, moderate MAI ratio of Bi-PeSC's at x=0.8 of MAI is the optimum sample due to uniform morphology, high V_{oc} (0.34 volts), good FF (30%) and a better efficiency value (0.0037%) as compared to other sample, which is suggested for further development of Bi-PeSC's. At the end, our research work may appreciate contribution towards the development of Pb-free perovskite solar cells field.

V. ACKNOWLEDGEMENT

The authors would like to express their gratitude to the Japanese government (via Monbukagakusho) for giving the

financial support to carried out this research work and unforgettable to Universiti Teknologi MARA (UiTM) for study supports.

VI. REFERENCES

Achoi, MF, Noman, MAA, Kato, S, Kishi, N & Soga, T 2021, 'Synthesis of bismuth triiodide nanofibers by spin-coating at room temperature', Materialia, vol. 16, pp. 101077.

Ataei, M, Adelifard, M & Hosseini, SS 2021, 'Physical Properties and Photovoltaic Performance of Perovskite Solar Cells Based on Lead-Free $A_3Bi_2I_9$ (A = CH_3NH_3, Cs) Active Layers', Journal of Electron Material, vol. 50, pp. 571–579.

Bresolin, BM, Hammouda, S Ben & Sillanpää, M 2019, 'Methylammonium iodo bismuthate perovskite $(CH_3NH_3)_3Bi_2I_9$ as new effective visible light-responsive photocatalyst for degradation of environment pollutants', Journal of Photochemistry Photobiology A Chemistry, vol. 376, pp. 116–126.

Chen, M, Wan, L, Kong, M, Hu, H 2018, 'Influence of rutile-TiO_2 nanorod arrays on Pb-free (CH3NH3)3Bi2I9-based hybrid perovskite solar cells fabricated through two-step sequential solution process', J. Alloy Compound, vol. 738, pp. 422-431.

Dhaouadi, M 2018, 'Physical properties of copper oxide thin films prepared by sol–gel spin–coating method', American Journal of Physics Applied, vol. 6, pp. 43.

Eperon, GE, Burlakov, VM, Docampo, P, Goriely, A & Snaith, HJ 2014, 'Morphological control for high performance, solution-processed planar heterojunction perovskite solar cells', Advanced Functional Material, vol. 24, pp. 151–157.

Green, MA, 1982, 'Solar cells, Operating Principles, Technology and System Application', The University of New South Wales, p. 97.

Hidzi, AH, Supee, A, Haladin, NB, Mohd Yusop, MZ & Wan Shamsuri, WN 2019, 'Role of Tartaric Acid on Structural, Morphological and Optical Properties of FeS_xO_y Films formed by Chemical Bath Depositi', Malaysian J. of Chemistry, vol. 21(3), pp. 110-116.

Hoye, RLZ, Brandt, RE, Osherov, A, Stevanovic, V, Stranks, SD, Wilson, MWB, Kim, H, Akey, AJ, Perkins, JD, Kurchin, RC, Poindexter, JR, Wang, EN, Bawendi, MG & Bulovic V 2016, 'Methylammonium Bismuth Iodide as a Lead-Free, Stable Hybrid Organic – Inorganic Solar Absorber', A Chemistry European Journal of Communication, vol. 80401, pp. 2605–2610.

Im, JH, Jang, IH, Pellet, N, Grätzel, M & Park, NG 2014, 'Growth of $CH_3NH_3PbI_3$ cuboids with controlled size for high-efficiency perovskite solar cells', National Nanotechnology, vol. 9, pp. 927–932.

Jain, SM, Phuyal, D, Davies, ML, Li, M, Philippe, B, Castro, CD, Qiu, Z, Kim, J, Watson, T, Tsoi, WC, Karis, O, Rensmo, H, Boschloo, G, Edvinsson, T & Durrant, JR 2018, 'An effective approach of vapour assisted morphological tailoring for reducing metal defect sites in lead-free, $(CH_3NH_3)_3Bi_2I_9$ bismuth-based perovskite solar cells for improved performance and long-term stability', Nano Energy, vol. 49, pp. 614–624.

Kawai, T, Ishii, A, Kitamuha, T, Shimanuki, S, Iwata, M, & Ishibashi, Y 1996, 'Optical Absorption in Band-Edge Region of $(CH_3NH_3)_3Bi_2I_9$ Single Crystals', Journal of the Physical Society of Japan', vol. 65, pp. 1464–1468.

Kubota, N 2001, 'Effect of impurities on the growth kinetics of crystals', Crystal Research Technology, vol. 36, pp. 749–769.

Lakhdar, N & Hima, A 2020, 'Electron transport material effect on performance of perovskite solar cells based on $CH_3NH_3GeI_3$', Optical Material (Amst), vol. 99, pp. 109517.

Lan, C, Luo, J, Zhao, S, Zhang, C, Liu, W, Hayase, S & Ma, T 2017, 'Effect of lead-free $(CH_3NH_3)_3Bi_2I_9$ perovskite addition on spectrum absorption and enhanced photovoltaic performance of bismuth triiodide solar cells', Journal of Alloys Compound, vol. 701, pp. 834–840.

Levchuk, I, Hou, Y, Gruber, M, Brandl, M, Herre, P, Tang, X, Hoegl, F, Batentschuk, M, Osvet, A, Hock, R, Peukert, W, Tykwinski, RR, and Brabec, CJ 2016, 'Deciphering the Role of Impurities in Methylammonium Iodide and Their Impact on the Performance of Perovskite Solar Cells', Advance Material Interfaces, vol. 3, pp. 1–10.

Li, H, Wu, C, Yan, Y, Chi, B, Pu, J, Li, J & Priya, S 2017, 'Fabrication of Lead-Free $(CH_3NH_3)_3Bi_2I_9$ Perovskite

Photovoltaics in Ethanol Solvent', ChemSusChem, vol. 10, pp. 3994–3998.

Limaye, MV, Chen, SC, Lee, CY, Chen, LY, Singh, SB, Shao, YC, Wang, YF, Hsieh, SH, Hsueh, HC, Chiou, JW, Chen, CH, Jang, LY, Cheng, CL, Pong, WF & Hu, YF 2015, 'Understanding of sub-band gap absorption of femtosecond-laser sulfur hyperdoped silicon using synchrotron-based techniques', Science Reports, vol. 5, pp. 1–12.

Liu, Z, Qiu, L, Juarez-Perez, EJ, Hawash, Z, Kim, T, Jiang, Y, Wu, Z, Raga, SR, Ono, LK, Liu, S & Qi, Y 2018, 'Gas-solid reaction based over one-micrometer thick stable perovskite films for efficient solar cells and modules', Natural Communications, vol. 9, pp. 3880.

Matiur, RM, Kato, S & Soga, T 2021, 'All-solution-processed environment-friendly solid-state BiOI photovoltaic cell with high-short-circuit current by successive ionic layer adsorption and reaction (SILAR)', J. Mater. Electron, vol. 32, pp. 18342-18350.

Mohammadian-Sarcheshmeh, H, Mazloum-Ardakani, M, Rameez, M, Shahbazi, S & Diau, EWG 2020, 'Application of a natural antioxidant as an efficient strategy to decrease the oxidation in Sn-based perovskites', Journal of Alloys Compound, vol. 846, pp. 156351.

Momblona, C, Kanda, H, Sutanto, AA, Mensi, M, Roldán-Carmona, C & Nazeeruddin, MK 2020, 'Co-evaporation as an optimal technique towards compact methylammonium bismuth iodide layers', Scientific Reports vol. 10, pp. 10640.

Öz, S, Hebig, JC, Jung, E, Singh, T, Lepcha, A, Olthof, S, Flohre, J, Gao, Y, German, R, Loosdrecht, PHMV, Meerholz, K, Kirchartz, T & Mathur, S 2016, 'Solar energy materials & solar cells applications', Solar Energy Material Solution, vol. 158, pp. 195–201.

Park, BW, Philippe, B, Zhang, X, Rensmo, H, Boschloo, G & Johansson, EMJ 2015, 'Bismuth based hybrid perovskites $A_3Bi_2I_9$ (A: Methylammonium or Cesium) for solar cell application', Advance Material, vol. 9, pp. 6806–6813.

Pujaru, S, Maji, P, Sadhukhan, P, Ray, A, Ghosh, B & Das, S 2020, 'Dielectric relaxation and charge conduction mechanism in mechanochemically synthesized methylammonium bismuth iodide', Journal of Material Science: Material Electron, vol. 31, pp. 8670–8679.

Ran, C, Wu, Z, Xi, J, Yuan, F, Dong, H, Lei, T, He, X & Hou, X 2017, 'Construction of compact methylammonium bismuth iodide film promoting lead-free inverted planar heterojunction organohalide solar cells with open-circuit voltage over 0.8V', Journal of Physical Chemistry Letters, vol. 8, pp. 394–400.

Sanders, S, Stümmler, D, Pfeiffer, P, Ackermann, N, Simkus, G, Heuken, M, Baumann, PK, Vescan, A & Kalisch, H 2018, 'Morphology control of organic–inorganic bismuth-based perovskites for solar cell application', Physical Status Solidi, vol. 215, pp. 1800409.

Shin, J, Kim, M, Jung, S, Kim, CS, Park, J, Song, A, Chung, KB, Jin, SH, Lee, JH & Song, M 2018, 'Enhanced efficiency in lead-free bismuth iodide with post treatment based on a hole-conductor-free perovskite solar cell', Nano Research, vol. 11, pp. 6283–6293.

Shirahata, Y 2020, 'Effects of annealing temperature on photovoltaic properties of lead-free $(CH_3NH_3)_3Bi_2I_9$ solar cells', Journal of Ceramics Society Japan, vol. 128, pp. 298–303.

Singh, T, Kulkarni, A, Ikegami, M & Miyasaka, T 2016, 'Effect of Electron Transporting Layer on Bismuth-Based Lead-Free Perovskite $(CH_3NH_3)_3$ Bi_2I_9 for Photovoltaic Applications', ACS Applied Material Interfaces, vol. 8, pp. 14542–14547.

Srivast, S, Singh, A, Kumar, P & Pradhan, B 2021, 'Comparative performance analysis of lead-free perovskite solar cells by numerical simulation', https://doi.org/10.21203/rs.3.rs-583148/v1.

Stümmler, D, Sanders, S, Mühlenbruch, S, Pfeiffer, P, Simkus, G, Heuken, M, Vescan, A & Kalisch, H 2019, 'Fabrication of methylammonium bismuth iodide layers employing methylamine vapor exposure', Physical Status Solidi Applied Material Science vol. 216, pp. 1900169.

Thornton, ST, Abdelmageed, G, Kahwagi, RF & Koleilat, GI 2021, 'Progress towards lead-free, efficient, and stable perovskite solar cells', J. Chem. Tech. And Biotech. vol.97, pp. 810-829.

Unlu, F, Kulkarni, A, Le, K, Bohr, C, Bliesener A, Oz, SD, Jena, AK, Ando, Y, Miyasaka, T, Kirchartz, T & Mathur, S 2020, 'Single- or double A-site cations in A3Bi2I9 bismuth perovskites: What is the suitable choice?', Journal of Materials Research, vol. 36, pp. 1794-1804.

Wang, H, Tian, J, Jiang, K, Zhang, Y, Fan, H, Huang, J, Yang, LM, Guan, B & Song, Y 2017, 'Fabrication of methylammonium bismuth iodide through interdiffusion of solution-processed BiI_3/CH_3NH_3I stacking layers', RSC Advances, vol. 7, pp. 43826–43830.

Wang, Y, Liu, Y, Xu, Y, Zhang, C, Bao, H, Wang, J, Guo, Z, Wan, L, Eder, D & Wang, S 2020, '$(CH_3NH_3)_3Bi_2I_9$ perovskite films fabricated via a two-stage electric-field-

assisted reactive deposition method for solar cells application', Electrochem. Acta, vol. 329, pp. 135173.

Zhang, W, Pathak, S, Sakai, N, Stergiopoulos, T, Nayak, PK, Noel, NK, Haghighirad, AA, Burlakov, VM, Dequilettes, DW, Sadhanala, A, Li, W, Wang, L, Ginger, DS, Friend, RH & Snaith, HJ 2015, 'Enhanced optoelectronic quality of perovskite thin films with hypophosphorous acid for planarheterojunction solar cells', Natural Communications, vol. 6, pp. 1–9.

Zhang, Z, Li, X, Xia, X, Wang, Z, Huang, Z, Lei, B & Gao, Y 2017, 'High-quality $(CH_3NH_3)_3Bi_2I_9$ film-based solar cells: pushing efficiency up to 1.64%', Journal of Physical Chemistry Letter, vol. 8, pp. 4300–4307.